Liquid Crystals
Publication details, including instructions for authors and subscription information:
http://www.informaworld.com/smpp/title~content=t713926090

In-situ monitoring of a film preparation process for hydroxypropyl cellulose cast from isotropic aqueous solution using microdielectrometry

Katsufumi Tanaka[a]; Yuichiro Tanabe[a]; Takatoshi Morina[b]; Ryuichi Akiyama[a]
[a] Department of Macromolecular Science and Engineering, Graduate School of Science and Technology, Kyoto Institute of Technology, Kyoto 606-8585, Japan [b] Department of Polymer Science and Engineering, Kyoto Institute of Technology, Kyoto 606-8585, Japan

To cite this Article Tanaka, Katsufumi , Tanabe, Yuichiro , Morina, Takatoshi and Akiyama, Ryuichi(2008) 'In-situ monitoring of a film preparation process for hydroxypropyl cellulose cast from isotropic aqueous solution using microdielectrometry', Liquid Crystals, 35: 3, 253 — 264
To link to this Article: DOI: 10.1080/02678290701862371
URL: http://dx.doi.org/10.1080/02678290701862371

Liquid Crystals,
Vol. 35, No. 3, March 2008, 253–264

Taylor & Francis
Taylor & Francis Group

In-situ monitoring of a film preparation process for hydroxypropyl cellulose cast from isotropic aqueous solution using microdielectrometry

Katsufumi Tanaka[a]*, Yuichiro Tanabe[a], Takatoshi Morina[b] and Ryuichi Akiyama[a]

[a]*Department of Macromolecular Science and Engineering, Graduate School of Science and Technology, Kyoto Institute of Technology, Matsugasaki, Kyoto 606-8585, Japan;* [b]*Department of Polymer Science and Engineering, Kyoto Institute of Technology, Matsugasaki, Kyoto 606-8585, Japan*

(Received 31 May 2007; final form 27 November 2007)

Solid cast films with polydomain textures were prepared on a glass substrate with transparent interdigitated electrodes from an isotropic aqueous solution of hydroxypropyl cellulose via its liquid crystalline phase under the sinusoidal electric field with small amplitude and frequency of $0.05\,V\,\mu m^{-1}$ and 10^5 Hz, respectively. The process was monitored using microdielectrometry as well as polarised optical microscopy. The apparent dielectric constant ε_r' and loss factor ε_r'' sensitively changed with time depending on the process conditions. On the other hand, the logarithmic relation between ε_r'' and ε_r' showed a single curve, when they were normalised by an effective portion of the electrostatic energy density estimated using each solid-film thickness. The conversion to the solid film was estimated during the process based on the concentration dependences of ε_r' and ε_r''. Characteristic times were reported for the onset of the biphasic phase, fully developed cholesteric phase and termination of the process.

Keywords: hydroxypropyl cellulose; aqueous solutions; cast films; *in-situ* monitoring; dielectric properties; optical observations; polydomain textures

1. Introduction

Hydroxypropyl cellulose (HPC) is known as a lyotropic liquid crystal with a cholesteric phase structure in concentrated solutions (*1, 2*). The critical concentration for the onset of the phase transition and coexistence of the isotropic–cholesteric phases was reported to be about 40 wt% at room temperature (*2–5*), and the upper concentration limit of the biphasic region has been reported to be slightly sensitive around room temperature, but also reported to be around 47 wt% at room temperature (*3–5*) or below about 18°C (see (*6*)). The solution became gel-like (or a highly viscous fluid in the cholesteric phase (*3*)) at concentrations higher than 70 wt%, and it became a clear film as the concentration was increased further (*2*).

In view of materials engineering, a similar phase behaviour would be reproduced during the preparation process of a solid film cast from an isotropic aqueous solution of HPC because the water solvent is removed from the wet film in solution. The HPC is concentrated during the process, so that the solid cast film would be prepared on a substrate from the isotropic solution via its liquid crystalline phase. It should be pointed out that the process is essentially non-equilibrium. However, the phase behaviour reported so far would be helpful for an accessible reference, at least locally, if the process conditions are moderate enough. Similar approximations have been employed for the *in-situ* monitoring of methanol solutions of HPC during solvent transportation and evaporation from the cover slip edge (*7*), the thermosetting of polymers during curing (*8–10*) and so on, the monitoring methods of which are discussed later.

Furthermore, it is known that a monodomain texture with homeotropic or homogeneous molecular alignment cannot easily be prepared for liquid crystalline polymers including HPC. Instead, the anisotropic solutions of liquid crystalline polymers essentially show polydomain textures in the quiescent state (*4*) and shear induced textures or the banded texture after shearing (*5, 11, 12*). As these macroscopic textures are closely related to the macroscopic physical properties, the preparation methods for the monodomain texture and for the solid film keeping such a texture are highly desirable. The application of the electric field during the preparation process is a possible method for the texture. At the same time, the *in-situ* monitoring of the preparation process of solid films is also desirable for the precise control of the textures.

The *in-situ* monitoring of methanol solutions of HPC sandwiched between a glass substrate and a cover slip was reported using polarised optical microscopy with diffusion couple geometry during

*Corresponding author. Email: ktanaka@kit.ac.jp

ISSN 0267-8292 print/ISSN 1366-5855 online

DOI: 10.1080/02678290701862371
http://www.informaworld.com

solvent transportation and evaporation from the cover slip edge (*7*). During the process, a stable microstructure was observed in which the interior of the sample remained isotropic followed by a cholesteric liquid crystalline band, followed by a crystalline band nearest the external surface. The apparent diffusion coefficient was estimated from the birefringent width. In the geometry, the solvent is allowed to diffuse away and evaporate only from the cover slip edge, while the solvent is allowed to evaporate from the surface of the wet film in most cases of cast film preparations.

Microdielectrometry was first introduced as a useful method for the *in-situ* monitoring of thermosetting polymers during and after curing, using a pair of very small planar interdigitated electrodes as a part of a silicon integrated circuit (*8, 9*). The electrode geometry is not affected by the contraction or expansion of the material (or by solvent evaporation from the surface of the wet film in our case). Furthermore, metal oxide–semiconductor field-effect transistors (MOSFETs) can be built into the microelectrode sensor, allowing the device to be operated down to 1 Hz with the use of an electronic feedback circuit. The *in-situ* monitoring with the sensor was employed for estimating the conversion of thermosetting polymers during curing (*10*). The complicated signal analysis for the microdielectric data was then avoided by simply using a sensor with planar interdigitated electrodes although the measured signals might be relatively small. At the same time, theoretical analyses were reported for the electric-field distribution above the sensor surface. Using sensors with planar interdigitated electrodes of gold on fused silica, the flow-induced fractionation in the liquid of a homopolymer (*13*) and the near-wall structure evolution of a model liquid crystal in the quiescent and flowing states were reported (*14*).

In the present paper, the microdielectrometry is used for the *in-situ* monitoring of the preparation process of a solid film cast from an isotropic aqueous solution of HPC under the sinusoidal electric field with small amplitude and frequency of $0.05\,\mathrm{V\,\mu m^{-1}}$ ($\mathrm{kV\,mm^{-1}}$) and 10^5 Hz, respectively. The small amplitude of the electric field is chosen to keep polydomain textures in the present study. (On the other hand, aligned textures would be prepared by the application of the large amplitude of the electric field, which has also been studied in our laboratory.) Polarised optical microscopy is also simultaneously applied using a glass substrate with transparent interdigitated electrodes without a cover slip. An estimation of the distribution and effective portion of the electrostatic energy density for our microelectrodes is discussed in Appendix A. Experimentally, the effective portion of the electrostatic energy density is investigated for the wet films with different film thicknesses. The logarithmic relations between the apparent dielectric constant ε_r' and loss factor ε_r'', and a scaling behaviour between the two parameters normalised by the effective portion of the electrostatic energy density are reported. Furthermore, the conversions to the solid film are estimated during the process based on the concentration dependences of ε_r' and ε_r'' (see (*5*)). Characteristic times are also reported for the onset of the biphasic phase, fully developed cholesteric phase and termination of the process.

2. Experimental details

HPC was purchased from Sigma-Aldrich, Inc. The weight-averaged molecular weight, M_w, was approximately 80,000, and the number averaged molecular weight, M_n, was approximately 10,000, with moles of substitution (MS) of 3.5. The details were reported in a previous paper (*5*). Distilled water was used to prepare the isotropic solutions with a polymer concentration of 30 wt%, the volume fraction of which was 0.27 assuming the density of HPC to be $1.17\,\mathrm{g\,cm^{-3}}$ (see (*15*)). The sample solutions were kept for at least three weeks in a desiccator at room temperature. The wet films of the solutions were applied at room temperature onto the microdielectric sensor described below using applicators for the thicknesses of the wet film (d_W) from 24 to 500 μm. The thickness of the solid films (d_D) was also measured using a dial gauge. The relation between d_W and d_D is shown in Figure 1, in which the least-squares fit, $d_D = 0.26 d_W$, is also shown. The room temperature and relative humidity were monitored using a digital thermo-hygrometer.

In the present study, glass substrates with transparent interdigitated electrodes of tin-doped indium oxide (ITO) were used as the microdielectric sensor. A schematic illustration of the electrodes and a dark field image of part of the electrodes are shown in Figure 2. (The ratio in Figure 2 (a) is not faithfully reproduced.) Four pairs of the ITO electrodes were sputtered on a glass slide with the gap distance between the electrodes of 50 μm (D). The width of the electrodes was 1.2 mm (W). The face-to-face length for a pair of high voltage (V^*) and ground (G) electrodes was 10.5 mm (L), and the paired electrodes are numbered as shown in the figure. (In practice, the electrodes were connected to V^* and G with some additional lengths, which would to some extent affect the distribution of the electric field near the edges.) The thickness of the ITO electrodes was approximately 30 nm (d_e). An illustration is also shown in

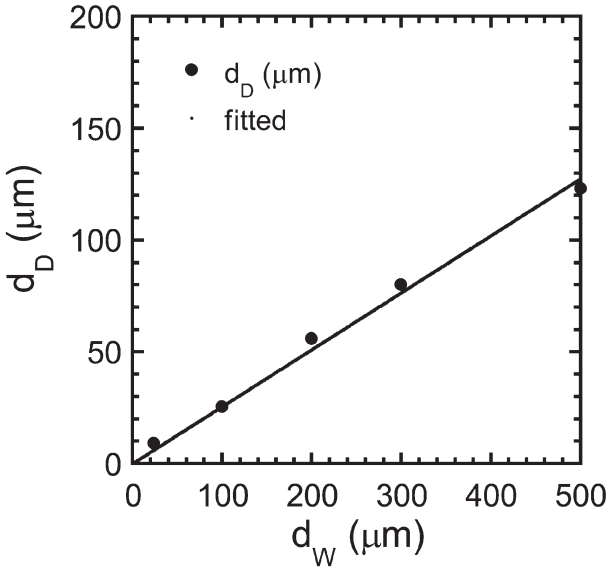

Figure 1. Relation between thickness of the solid film, d_D, and that of the wet film, d_W. The least-squares fit, $d_D=0.26d_W$, is also shown.

Figure 3 during the preparation process of the solid film cast from an isotropic aqueous solution of HPC. In the process, the thickness of the wet film is gradually decreased as the solvent is removed. Therefore, an estimation of the distribution and effective portion of the electrostatic energy density for our microelectrodes is briefly discussed in Appendix A. A characteristic (or penetration) depth of the electrostatic energy density above the microelectrodes is estimated to be on the order of the gap between the electrodes (D).

The sinusoidal electric field with small amplitude and frequency of 0.05 V μm^{-1} (kV mm^{-1}) and 10^5 Hz, respectively, was applied using a signal generator (NF, 1940) to the wet films during the process. For calculation of the dielectric parameters, the root-mean-squared amplitude (R) of the responding voltage (V_m*) to the applied sinusoidal voltage (V*), and the phase difference (θ) between V* and V_m* shown in Figure 4 was measured using a digital lock-in amplifier (NF, LI5640). These data were transferred to a PC. The system for the dielectric measurements was calibrated using the parallel combination of a resistor and capacitor, the calibration of which was also made using an impedance analyser (HP, 4192A). The capacitance (C_s) and conductance (G_s) of the sample were then calculated assuming the linear combination of the capacitance and conductance. (The contribution of the glass substrate was removed after calibration with a reference sample as discussed below.) A series of resistors with R_k of 1000 Ω and R_0 of 1 Ω was used so

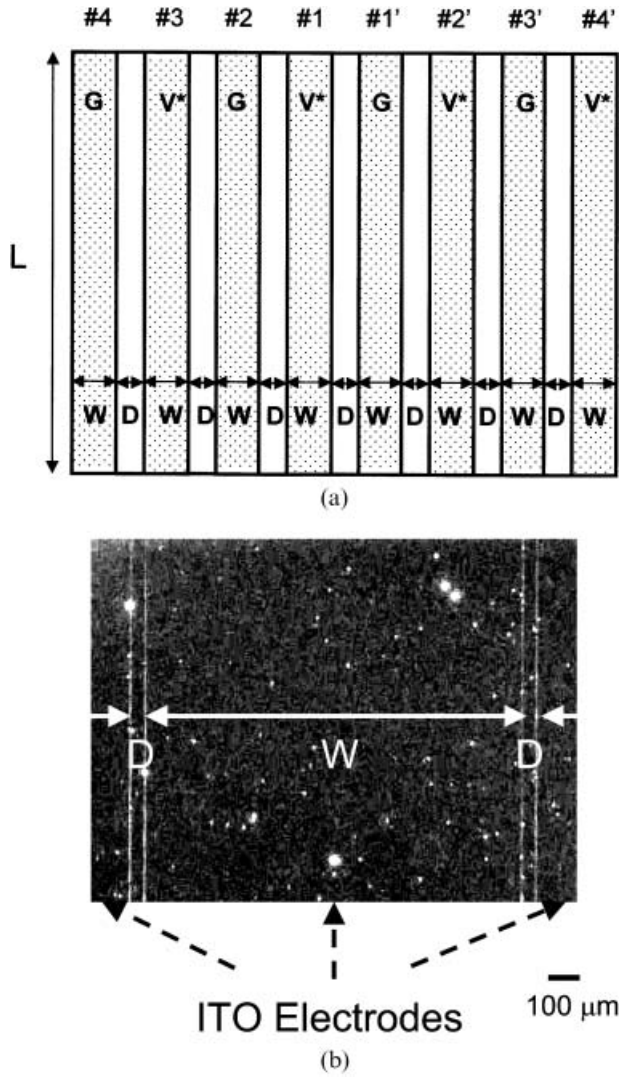

Figure 2. (a) Schematic illustration of the top view of the transparent interdigitated electrodes deposited on a glass substrate and (b) a dark field image of part of the electrodes. In (a), four pairs of electrodes with the width W and length L for high voltage (V*) and ground (G) are numbered. The gap distance between the electrodes is denoted by D. The ratio in (a) is not faithfully reproduced.

that the responding voltage was not larger than 1 V. (The resistances were independent of the frequency below 10^6 Hz.)

The apparent dielectric constant, ε_r', and loss factor, ε_r'', of the wet film at a frequency of 10^5 Hz were calculated during the process using the following equations:

$$\varepsilon_r'/\varepsilon_{ref}' = (C_s - C_f)/(C_{ref} - C_f), \quad (1)$$

$$\varepsilon_r''/\varepsilon_{ref}' = G_s/[2\pi v(C_{ref} - C_f)], \quad (2)$$

where C_{ref} and ε_{ref}' are the capacitance and the

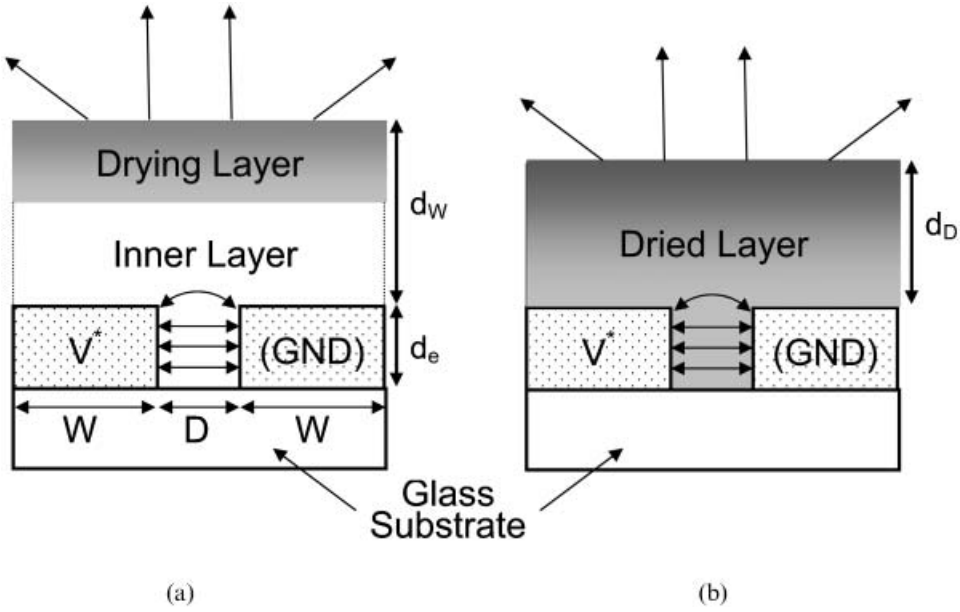

Figure 3. Schematic illustration of the side view of part of the solution on the electrodes (substrate) (a) immediately after application of the wet film and (b) just before the termination of the process.

dielectric constant of the reference sample, respectively, and v is the frequency. Before each measurement, C_f was determined for calibration using Equation (1) with a reference sample having a well-defined temperature dependence of ε_{ref}'. In the present study, air and sufficiently dried hexane (*16*) were used for the calibration. For the calibration using hexane, the microelectrode was completely immersed in the hexane-containing bottle.

The anisotropic texture was observed at room temperature using a polarised optical microscope with cross polarisors (Nikon, Eclipse E600W Pol) equipped with a CCD camera. Dark field images of the microelectrodes were also observed using an optical microscope (Nikon, Eclipse E600W) equipped with a CCD camera. The image data were recorded on a hard disk using a digital video recorder and transferred to a PC.

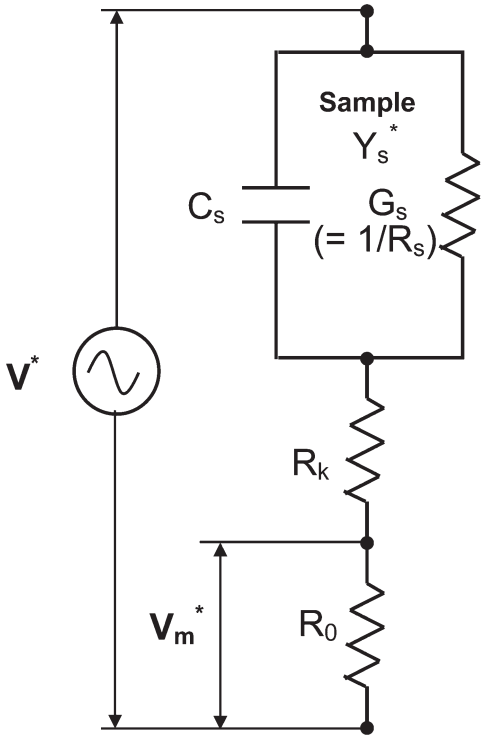

Figure 4. An equivalent circuit used for the dielectric measurements.

3. Results and discussion

3.1. *Optical observations and dielectric measurements during the process*

During the preparation process of a solid film cast from an isotropic aqueous solution of HPC, the water solvent is removed from the wet film of the solution. The HPC is concentrated, so that the solid cast film would be prepared on a substrate from the isotropic solution via its liquid crystalline phase. In the present study, it is assumed that similar concentration dependences of ε_r' and ε_r'' as measured in a liquid cell (*5*) are reproduced for estimating the conversion to the solid film.

In Figure 5, the dielectric constant (Figure 5 (a)) and loss factor (Figure 5 (b)) measured at 10^5 Hz for the HPC aqueous solutions and the least-squares fits are plotted against the polymer concentration. In the

Figure, the data from (*5*) are used, and the reported onset concentration of the mesophase formation and the coexistence of the isotropic and ordered phases is indicated by the broken line b. The upper concentration limit of the biphasic phase is also indicated by the broken line c (see (*2–5*)). The ε_r' data above the concentration c of 10 wt% can be linearly fitted as $\varepsilon_r' = 102.7 - 0.9359c$. The ε_r'' data are fitted as Fit1, $\varepsilon_r'' = 205.1c\exp(-0.0009379c^2)$, and as Fit2, $\varepsilon_r'' = 0.00778\ (100-c)^3$ above 30 wt%. The function assumed for ε_r' is linear and the fit is good, which would be favourable for estimating the conversion to the solid film during the process. On the other hand, the functions assumed for ε_r'' are not linear and the changes in ε_r'' are much larger than those in ε_r', so

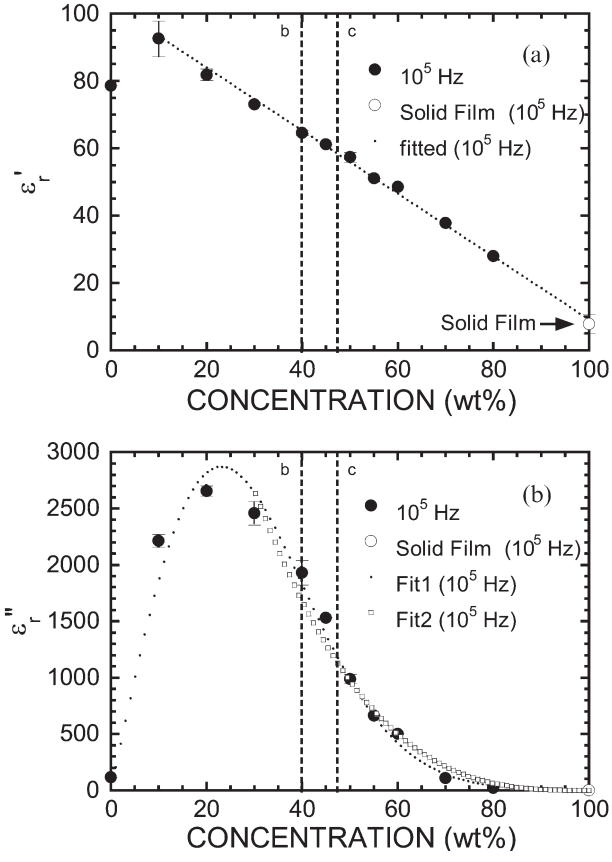

Figure 5. (a) The dielectric constant and (b) the loss factor measured at 10^5 Hz for the HPC aqueous solutions and the least-squares fits plotted against the polymer concentration. The data from (*5*) are used and the reported onset concentration of the mesophase formation and the coexistence of the isotropic and ordered phases are indicated by the broken line b. The upper concentration limit of the biphasic phase is also indicated by the broken line c (see (*2–5*)). The ε_r' data above the concentration c of 10 wt% are fitted as $\varepsilon_r' = 102.7 - 0.9359c$. The ε_r'' data are fitted as Fit1, $\varepsilon_r'' = 205.1c\ \exp(-0.0009379c^2)$, and as Fit2, $\varepsilon_r'' = 0.00778\ (100-c)^3$ above 30 wt%.

that the errors of the fits are not necessarily negligible.

The HPC molecules act like partially flexible rods in aqueous solutions because of the intra-molecular hydrogen bonding. For aqueous solutions of HPC (*5*), the dielectric relaxation at lower frequencies was affected by the electrode polarisation and the conduction (or apparent dielectric polarisation) of ionic species dissolved from HPC, and important relaxations including the rotational diffusion about minor axis (the longitudinal rotation) of a partially flexible rod were screened out. On the other hand, the rotational diffusion of the partially flexible rod with side chains about the major axis (the transversal rotation) responded at higher frequencies. The local motion of chain segments in the relatively flexible rod was also detected as a longitudinal component and/or transversal component even confined in the concentrated solutions.

For the solution of 70 wt%, ε_r'' (or ε_r') at lower frequencies showed a typical frequency dependence suggesting the effect of the dc conduction (or the electrode polarisation). The corrected portions of ε_r'(corrected) and ε_r''(corrected) plotted logarithmically against frequency showed broad relaxations around 10^6 Hz and at frequencies lower than 10^4 Hz. From our discussion in (*5*), the broad relaxation at the lower frequencies was partially related to the limited angular diffusion of a rod (the longitudinal rotation) within a virtual cone (see (*17*) and references therein). The relaxation around 10^6 Hz was related to the transversal rotational diffusion of a partially flexible rod with side chains as well as a local motion of chain segments confined in the concentrated solution (*18, 19*). Similar relaxations were reported even for the solid films of HPC with the primary dispersion (α_a) around 4×10^2 Hz or lower at 290 K (see (*20*)), and with an overlapped secondary dispersion of β and γ relaxations around 5×10^5 Hz at 290 K (see (*21*)).

It is worthwhile to note that ε_r''(corrected) showed a local minimum around 10^4–10^5 Hz (see (*5*)). Therefore, the transversal rotational diffusion of a partially flexible rod with side chains as well as the local motion of chain segments can still be active at 10^5 Hz for the solutions and also for the solid films. In this case, ε_r' at 10^5 Hz simply depends on the volume (or weight) fraction of HPC giving the linear dependence after the maximum shown in Figure 5 (a). (In addition, ε_r' at 10^6 Hz decreased linearly as the concentration increased from 0 wt% to around 47 wt%, and ε_r' above 47 wt% further decreased linearly but a little more steeply.)

In the present study, ε_r'' shown in Figure 5 (b) is not corrected and ε_r'' is mainly related to the

conductance of the sample at 10^5 Hz. Furthermore, no remarkable changes in the concentration at the maximum for ε_r'' were observed at 10^6 Hz (see (*5*)). The initial increases in ε_r'' shown in Figure 5 (b) are related to the increase in the ionic species dissolved from HPC, which contribute to the ionic conduction (or apparent dielectric polarisation at the frequency). The gradual decrease after the maximum up to 45 wt% would be related to the decreases in water and the dissociation of the ionic species. The increase in the solution viscosity with an increase in the concentration of HPC would also be a factor for the decrease. At concentrations around 45 wt% in the biphasic region, small anisotropic spherulites were dominant, but an isotropic portion surrounding the anisotropic spherulites would act as a conduction path. Above 47 wt%, at which the cholesteric phase fully developed, the ionic species are forced to move across the boundary between the polydomain textures with potential barriers for the conduction. The potential barriers (or electrical inhomogeneities) would contribute to produce specially separated charges temporarily, and also contribute significantly to the conduction losses (or contribute additionally to the apparent dielectric polarisation, but the contribution was minor in the present case; see (*22*) and references therein). In the fully developed cholesteric phase, the molecular motions were also restricted. The potential barriers for the ionic conduction as well as the restriction for the molecular motions, especially for the longitudinal rotation, would significantly be increased above 47 wt% in the fully developed cholesteric phase with the polydomain textures (*5*).

In Figure 6, captured images are shown during the preparation process of a solid film with a d_D of 87 μm, which were observed using a polarised optical microscope. As shown in Figure 6 (a), the just applied wet film was isotropic. The onset of the appearance of the anisotropic domains is found in the image taken at 1040 s (Figure 6 (b)). Fully developed anisotropic domains in the polydomain texture can be seen in the image taken at 1600 s (Figure 6 (c)). No difference in the images after 1600 s can easily be found although the solvent was further removed from the wet film after 1600 s. Therefore, the onset of the appearance of the anisotropic domains would be detectable, while the termination of the process cannot conclusively be determined only by polarised optical microscopy. Furthermore, the thickness of the film was important for observation of the anisotropic domains. For instance, the anisotropic domains for the films thinner than the d_D of 24 μm were not observed in the present study. It should also be pointed out that the anisotropic domains are relatively small and randomly distributed so that the sample can be macroscopically assumed to be homogeneous.

In Figure 7, the amplitude, R, and the phase angle, θ, during the casting process are shown for the d_D of 87 μm (Figure 7 (a)) and for the d_D of 53 μm (Figure 7 (b)). In Figure 7 (a), the times corresponding to Figures 6 (b), (c) and (d) are indicated by the arrows b, c and d, respectively. The arrows indicate the same values similarly in Figure 7 (b). In both cases, R is initially large and gradually decreases during the process, followed by saturation. On the other hand, θ is initially small and increases gradually, followed by saturation. In Figure 7 (a), the changes in R and θ are not pronounced around the onset time of the appearance of the anisotropic domains, which is indicated by the arrow b. The positions indicated by the arrows for the film with the d_D of 53 μm are slightly delayed in Figure 7 (b).

Qualitatively, the wet films of the just applied HPC aqueous solution were conductive with a large amplitude and a small phase difference, while the solid films were capacitive with a small amplitude and a large phase difference. For engineering applications to monitor the process qualitatively and just determine the termination, it would be satisfactory that the termination of the process is easily determined only by monitoring the phase difference. Based on the concentration dependences of ε_r' and ε_r'' shown in Figure 5, the conversion to the solid film would be estimated during the process by monitoring the apparent dielectric constant, ε_r', and loss factor, ε_r'', which are discussed later.

3.2. *Relation between the apparent dielectric constant and loss factor and a scaling behaviour*

Figure 8 shows the apparent dielectric constant (Figure 8 (a)) and loss factor (Figure 8 (b)) measured at 10^5 Hz for the wet films with different film thicknesses during the casting process. For the following discussion, the thicknesses of the solid films are shown in the Figure. The time for the termination of the process gradually increases as the film thickness increases. Changes in the apparent dielectric constant, ε_r', and loss factor, ε_r'', during the process were sensitive to the process conditions, especially to the ambient humidity. In the Figure, the curves of ε_r' (or ε_r'') for the d_D of 52 and 53 μm are not superposed although the sold-film thicknesses are similar. The ambient temperatures for the two cases were almost the same around 19°C, while the humidity was slightly different. The humidity for the d_D of 53 μm was 40.4%RH. On the other hand, the humidity for the d_D of 52 μm was 45.3%RH, at

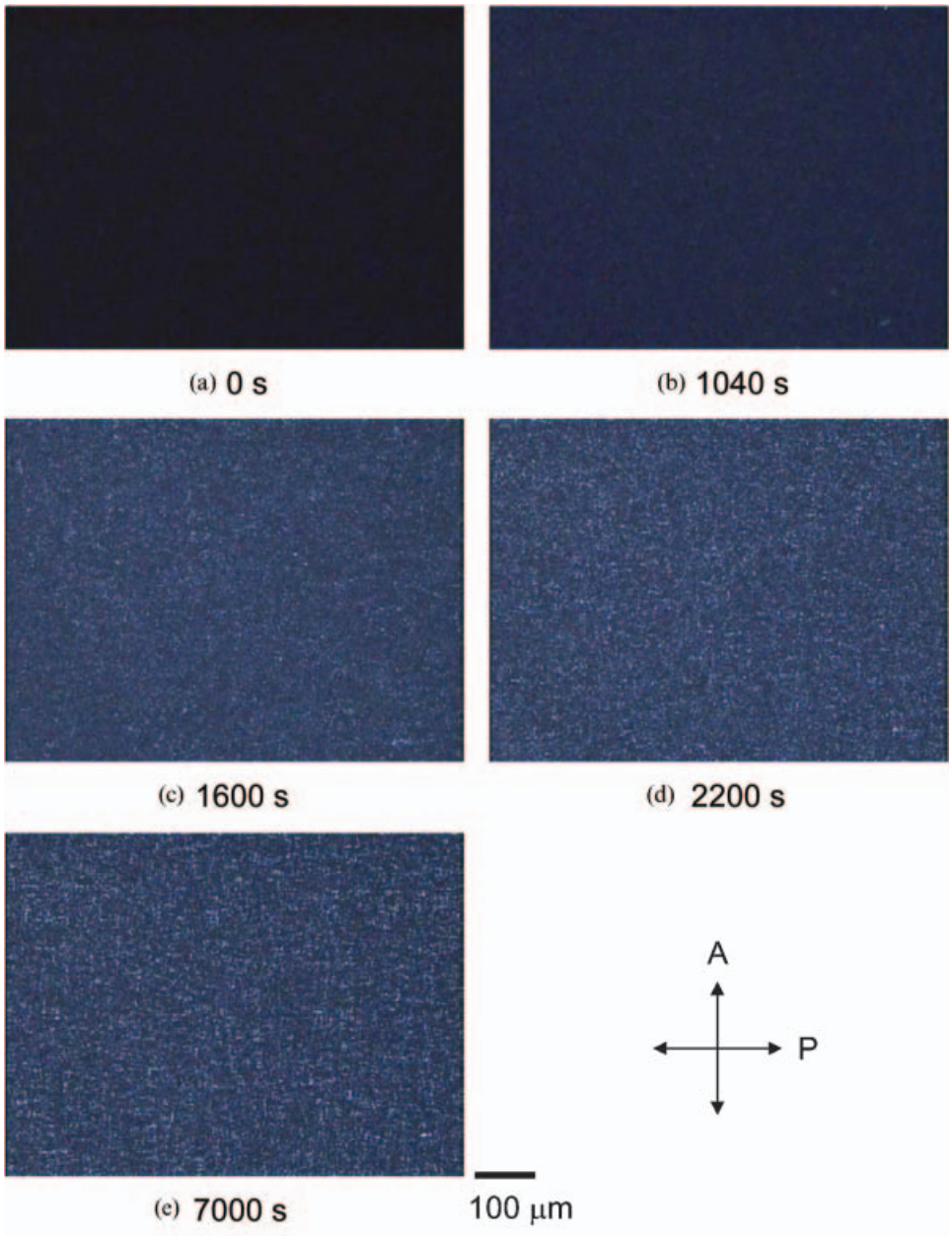

Figure 6. Captured images of the solution of HPC during the casting process for a solid film with a d_D of 87 μm observed using a polarised optical microscope.

which the slower changes in ε_r' (or ε_r'') can be seen in Figure 8.

Furthermore, the initial values of ε_r' in Figure 8 are obviously lower for the thinner films of the d_D of 9 and 24 μm, while the differences in the initial values of ε_r'' are not so pronounced. As discussed in Appendix A, a characteristic (or penetration) depth of the electrostatic energy density above the microelectrodes is estimated to be half the gap distance between the electrodes, i.e. 25 μm. Therefore, the electric field would penetrate the thin films with the d_D of 9 and 24 μm, and the contribution of air above the films to ε_r' was not negligible. On the other hand, the wet film initially appeared to be highly conductive, which would be favourable for the evaluation of ε_r''.

The logarithmic relations between ε_r'' and ε_r' shown in Figure 8 are plotted in Figure 9 (a). The data above 30 wt% including the solid film shown in Figure 5 are also plotted as a reference. Interestingly, the logarithmic relations between ε_r'' and ε_r' for the thicker films appear to show a single curve, which includes the curves for the d_D of 52 and 53 μm. However, the curves for the thinner films are not superposed on the curve. Instead, a similar relation is plotted in Figure 9 (b)

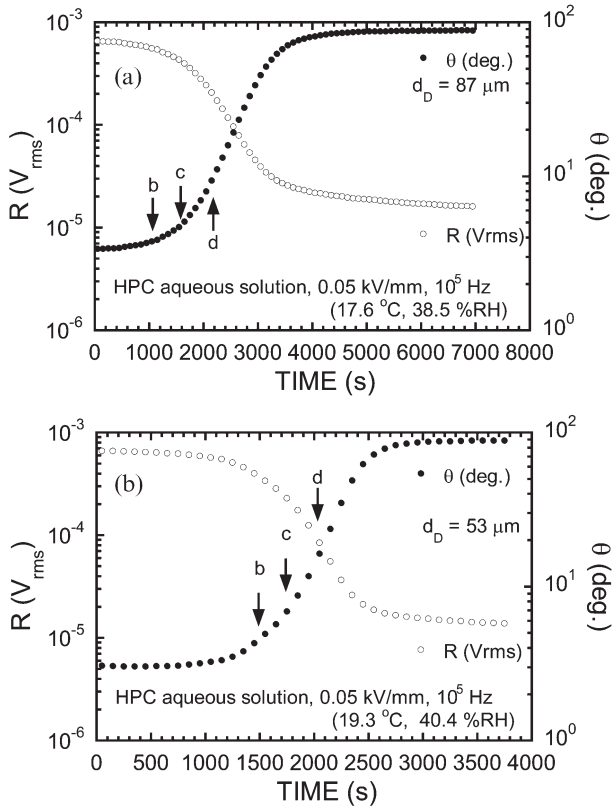

Figure 7. Amplitude, R, and phase angle, θ, during the casting process for the d_D of (a) 87 μm and (b) 53 μm. The times corresponding to figures 6(b), (c) and (d) are indicated by the arrows b, c and d, respectively.

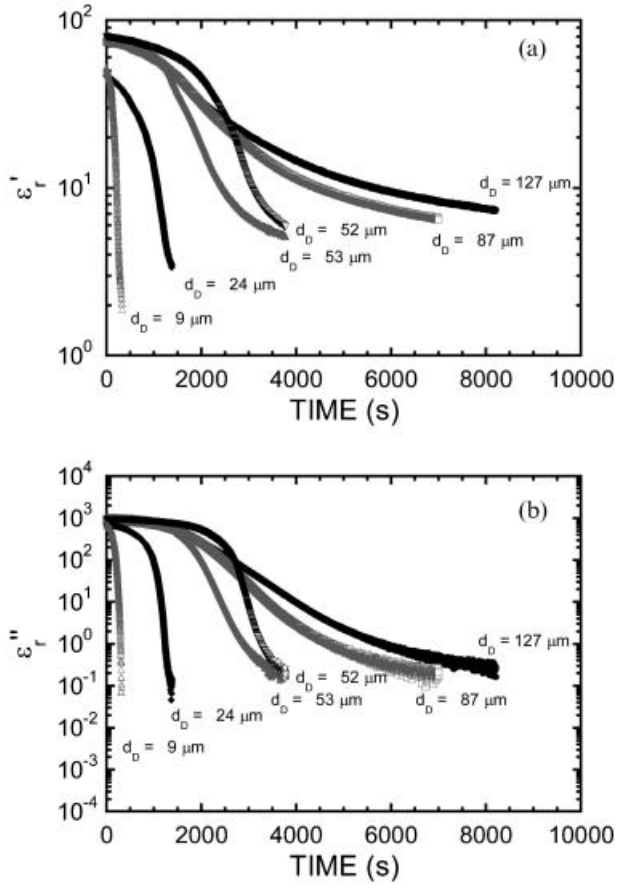

Figure 8. (a) The apparent dielectric constant and (b) loss factor measured at 10^5 Hz for the solutions during the casting process. The thicknesses of the solid films are also shown.

between the two parameters normalised by an effective portion of the electrostatic energy density, $J(d_D/D)$, calculated in Appendix A. In Figure 9(b), a single curve can be seen, which includes the thinner films. The normalised dielectric constant $\varepsilon_r'/J(d_D/D)$ just before the termination of the process is in good agreement with the dielectric constant for the solid film, while $\varepsilon_r''/J(d_D/D)$ appears to be slightly smaller than ε_r'' for the solid film on the logarithmic scale. (In addition, ε_r' and ε_r'' of the solid film are averaged values and experimental errors are not plotted in Figure 9(b).) In fact, the corrections for the logarithmic relation between $\varepsilon_r''/J(d_D/D)$ and $\varepsilon_r'/J(d_D/D)$ may not be perfect, and the data in Figure 9(b) are somewhat scattered. Technically, one of the reasons for the error is that the evaluation of $J(d_D/D)$ is based only on d_D. Further, the changes in ε_r'' are extremely large, so that the errors of the corrections are not necessarily negligible. Practically, the corrections in the present study would be satisfactory for the first step to apply the present method to the *in-situ* monitoring of the drying process. The normalised dielectric constant $\varepsilon_r'/J(d_D/D)$ for the d_D of 9 μm at the initial stage is obviously overestimated, because the calculation of $J(d_D/D)$ is based only on d_D while the parameter z/D in equation (A3) decreases from d_W/D of 24/50 to d_D/D of 9/50, the values of which are smaller than the characteristic (or penetration) depth of the electrostatic energy density $(d/D)_{1/2}$ of 1/2. The evaluation of $J(z/D)$ can be improved with the *in-situ* monitoring for the thickness of the wet film during the process. Further study is needed to investigate the problem in detail.

As a whole, the logarithmic relation between $\varepsilon_r''/J(d_D/D)$ and $\varepsilon_r'/J(d_D/D)$ shown in Figure 9(b) agrees well with the reference curve except for the initial stage of the process for the thinner films. Therefore, the logarithmic relation between $\varepsilon_r''/J(d_D/D)$ and $\varepsilon_r'/J(d_D/D)$ would be approximately determined by the concentration within the characteristic (or penetration) depth of the electrostatic energy density $(d/D)_{1/2}$ during the process. The conversion to the solid film will be estimated during the process in the next section.

3.3. *Conversions to the solid film during the process*

In Figure 10, the conversion to the solid film is shown during the casting process for the d_D of 87 μm, which

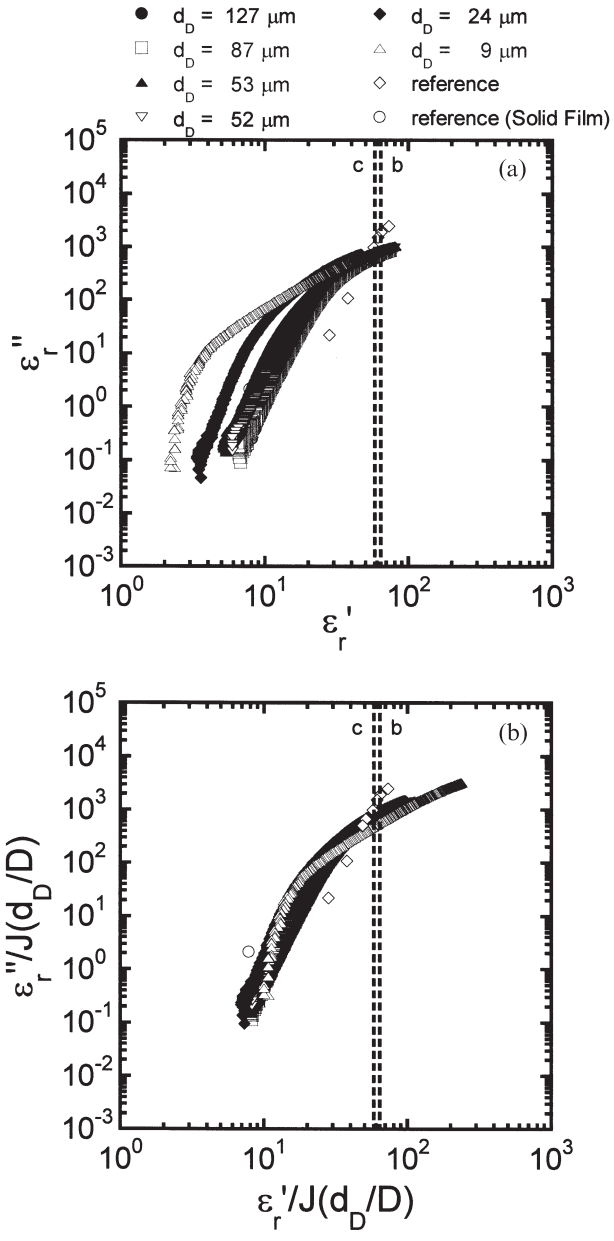

Figure 9. (a) The logarithmic relations between ε_r'' and ε_r' shown in Figure 9 and (b) a similar relation between the two parameters normalised by an effective portion of the electrostatic energy density, $J(d_D/D)$, calculated in Appendix A. The data above 30 wt% including the solid film shown in Figure 5 are also plotted as a reference.

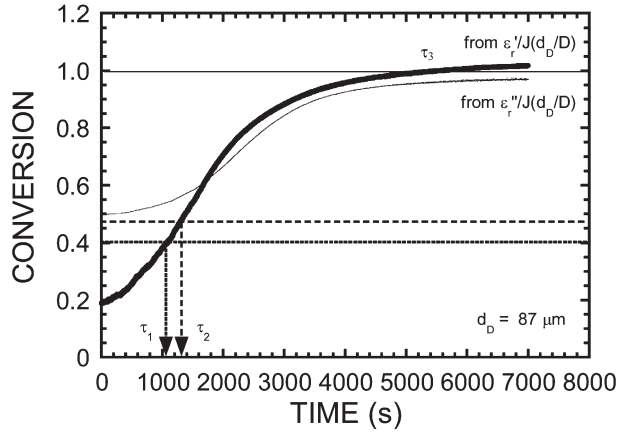

Figure 10. Conversions to the solid film during the casting process for the d_D of 87 μm calculated using the normalised data of $\varepsilon_r'/J(d_D/D)$ and a linear experimental relation shown in Figure 5 (a) and the normalised data of $\varepsilon_r''/J(d_D/D)$ and experimental relation of Fit2 shown in Figure 5 (b). The conversion is defined as $c/100$. Characteristic times are also shown for the onset of the mesophase formation and the coexistence of the isotropic and ordered phases, τ_1, fully developed cholesteric phase, τ_2, and termination of the casting process, τ_3.

was calculated using the normalised data of $\varepsilon_r'/J(d_D/D)$ and a linear experimental relation shown in Figure 5 (a). Furthermore, the conversion is also compared, which was calculated using the normalised data of $\varepsilon_r''/J(d_D/D)$ and experimental relation of Fit2 shown in Figure 5 (b). The conversion is defined as $c/100$. In the Figure, the reported onset conversion of the mesophase formation and the coexistence of the isotropic and ordered phases is indicated by the dotted line, and the upper concentration limit of the biphasic phase is indicated by the broken line (*2–5*). The full conversion is also indicated by the solid line. The calculated conversion slightly exceeds the reference value for the full conversion because the dielectric constant of the solid film depends on the ambient humidity (*18*) and the humidity was not exactly the same for the casting process. There can be systematic errors from the overestimation of the corrected values of $\varepsilon_r'/J(d_D/D)$ and $\varepsilon_r''/J(d_D/D)$ especially at the initial stage, and from errors of the fittings shown in Figure 5. In the case of the overestimation of the corrected values at the initial stage, the conversion at the initial stage can be underestimated. Sometimes, the conversion may be calculated to be negative. On the other hand, the conversion can be overestimated (or underestimated) in the case of the overestimation (or underestimation) of the fittings against the measured values using the linear fittings shown in Figure 5 (a) and Fit2 in Figure 5 (b). Experimentally, it takes some time to get the data after applications of the wet films, and the changes in ε_r'' are extremely large and rapid. Therefore, no definite reasons for the errors of ε_r'' were evaluated especially at the initial stage.

Characteristic times are also shown in the Figure for the onset of the mesophase formation and the coexistence of the isotropic and ordered phases, τ_1, the fully developed cholesteric phase, τ_2, and termination of the casting process, τ_3. The characteristic times of τ_1 and τ_2 determined by the conversion from

$\varepsilon_r'/J(d_D/D)$ agree fairly well with the polarised optical microscopy observations. On the other hand, the characteristic times of τ_1 and τ_2 cannot be determined by the conversion from $\varepsilon_r''/J(d_D/D)$ because the errors, possible reasons for which were discussed above, would contribute unfavourably to the estimation of the conversion from $\varepsilon_r''/J(d_D/D)$ in the present study. Furthermore, the characteristic time of τ_3 cannot be determined from $\varepsilon_r''/J(d_D/D)$ because the conversion around the termination was slightly underestimated using Fit2. In the following discussion, our attention is focused on the conversions from $\varepsilon_r'/J(d_D/D)$.

In Figure 11, conversions to the solid films are plotted semi-logarithmically against time during the casting process calculated using the normalised data of $\varepsilon_r'/J(d_D/D)$ and the linear experimental relation shown in Figure 5 (a). (In Figure 11, some conversions at the initial stage are calculated to be negative because of the overestimation of $\varepsilon_r'/J(d_D/D)$ for the thin film for the d_D of 9 μm, and the errors of the fits or measured data for the d_D of 52 and 53 μm.) As discussed in Figure 8, the time for the termination of the process gradually increases as the film thickness increases. Furthermore, the curves for the d_D of 52 and 53 μm can be distinguished in terms of the conversion, and the characteristic times can be determined in a comparable manner. The characteristic times are plotted in Figure 12 against the thickness of the solid film. Furthermore, the characteristic times observed using the polarised optical microscopy are also plotted in Figure 12. For instance, τ_b, τ_c and τ_d, correspond to the times as shown in Figures 6 (b), (c) and (d), respectively. In Figure 12, τ_1 and τ_2 agree fairly well with τ_b and τ_c, respectively, except for the two thinner films because the retardations were too small for polarised optical microscopy. Furthermore, τ_3 for the termination of the process shows almost a linear relation against d_D, the characteristic time of which cannot be conclusively determined only by polarised optical microscopy. On the other hand, the direct observations of the anisotropic textures would also be useful and helpful using polarised optical microscopy. Therefore, the simultaneous application of microdielectrometry and polarised optical microscopy would be highly effective for the *in-situ* monitoring of the casting process.

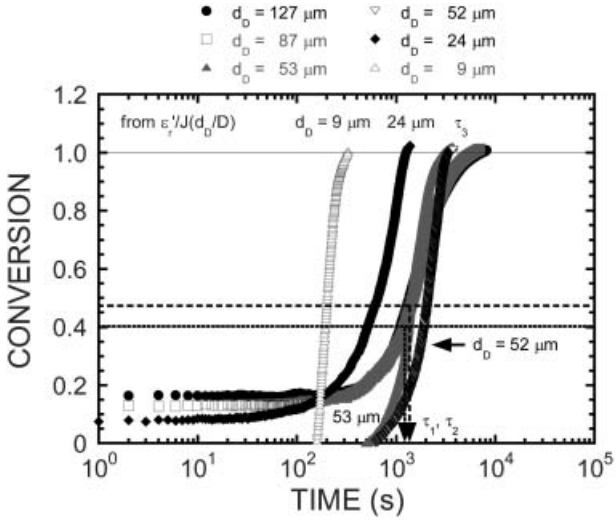

Figure 11. Conversions to the solid films during the casting process calculated using the normalised data of $\varepsilon_r'/J(d_D/D)$ and the linear experimental relation shown in Figure 5 (a). Characteristic times of τ_1, τ_2 and τ_3 are also shown.

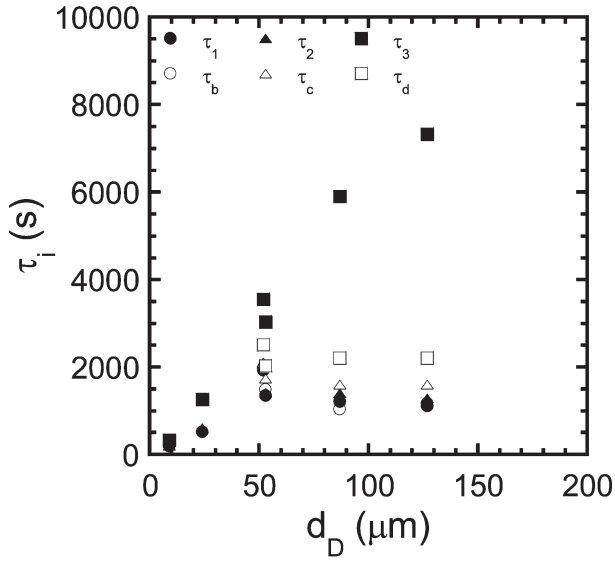

Figure 12. Characteristic times of τ_1, τ_2 and τ_3 plotted against the thickness of the solid film. The characteristic times observed using polarised optical microscopy are also plotted. For instance, τ_b, τ_c and τ_d, correspond to the times shown in Figures 6 (b), (c) and (d), respectively.

Finally, the logarithmic relation between $\varepsilon_r''/J(d_D/D)$ and $\varepsilon_r'/J(d_D/D)$ shown in Figure 9 (b) suggests that the sample within the characteristic (or penetration) depth of the electrostatic energy density $(d/D)_{1/2}$ is mainly affected by the electric field during the process. The electrical orientation of anisotropic domains is also expected by application of the large amplitude of the electric field in a film with thickness on the order of $(d/D)_{1/2}$, the results of which will be reported in a subsequent paper.

4. Conclusions

In the present study, *in-situ* monitoring was investigated for the preparation process of the solid cast films with polydomain textures from an isotropic

aqueous solution of HPC via its liquid crystalline phase. The process was monitored using microdielectrometry as well as polarised optical microscopy. The apparent dielectric constant ε_r' and loss factor ε_r'' sensitively changed with time depending on the process conditions. On the other hand, the logarithmic relation between ε_r'' and ε_r' showed a single curve when they were normalised by an effective portion of the electrostatic energy density estimated using each solid-film thickness. The conversion to the solid film was estimated during the process based on the concentration dependences of ε_r' and ε_r''. Characteristic times were determined for the onset of the biphasic phase, fully developed cholesteric phase and termination of the process by microdielectrometry as well as polarised optical microscopy, while the characteristic time for termination of the process was not conclusively determined by polarised optical microscopy alone. It was demonstrated that simultaneous application of microdielectrometry and polarised optical microscopy was highly effective for *in-situ* monitoring of the casting process in the present study.

Acknowledgement

This work was partially supported by a Grant-in-Aid for Scientific Research from Japan Society for the Promotion of Science.

References

(1) Werbowyj R.S.; Gray D.G. *Mol. Cryst. Liq. Cryst.,* **1976**, *34*, 97–103.
(2) Werbowyj R.S.; Gray D.G. *Macromolecules* **1980**, *13*, 69–73.
(3) Conio G.; Bianchi E.; Ciferri A.; Tealdi A.; Aden M.A. *Macromolecules* **1983**, *16*, 1264–1270.
(4) Fried F.; Sixou P. *J. Polym. Sci. Polym. Chem. Ed.* **1984**, *22*, 239–247.
(5) Tanaka K.; Morina T.; Tanabe Y.; Akiyama R. *Liq. Cryst.*, **2007**, *34*, 1019–1028.
(6) Guido S. *Macromolecules* **1995**, *28*, 4530–4539.
(7) Aronson C.L.; Catalogna J.C.; Webster W.D. *Polym. Bull.* **2004**, *53*, 43–52.
(8) Sheppard N.F.; Day D.R.; Lee H.L.; Senturia S.D. *Sens. Actuators* **1982**, *2*, 263–274.
(9) Senturia S.D.; Sheppard N.F. Jr.; Lee H.L.; Day D.R. *J. Adhesion* **1982**, *15*, 69–90.
(10) Eloundou J.P.; Ayina O.; Nga H.N.; Gerard J.F.; Pascault J.P.; Boiteux G.; Seytre G. *J. Polym. Sci. Part B* **1998**, *36*, 2911–2921.
(11) Riti J.-B.; Navard P. *J. Rheol.* **1998**, *42*, 225–237.
(12) Tanaka K.; Yonetake K.; Masuko T.; Akiyama R. *J. Macromol. Sci. Part B* **2003**, *42*, 901–914.
(13) Fodor J.; Hill D.A. *Macromolecules* **1992**, *25*, 3511–3520.
(14) Fodor J.S.; Hill D.A. *J. Rheol.* **1994**, *38*, 1071–1100.
(15) Samuels R.J. *J. Polym. Sci. Part A-2* **1969**, *7*, 1197–1258.
(16) Weast R.C. (Eds), *CRC Handbook of Chemistry and Physics* **1976–1977** 57th edn, CRC Press: Cleveland, OH, 1976–1977.
(17) Moteleb M.M.A.; Naoum M.M.; Shalaby M.M.; Saad G.R. *Polym. Int.* **1994**, *34*, 363–367.
(18) Shinouda H.G.; Moteleb M.M.A. *J. Appl. Polym. Sci.* **2005**, *98*, 571–582.
(19) Meiβner D.; Einfeldt J.; Kwasniewski A. *J. Non-Cryst. Solids* **2000**, *275*, 199–209.
(20) Pizzoli M.; Scandola M.; Ceccorulli G. *Plastics, Rubber Composites Process. Appl.* **1991**, *16*, 239–244.
(21) Rachocki A.; Markiewicz E.; Tritt-Goc J. *Acta Physica Polonica A* **2005**, *108*, 137–145.
(22) Einfeldt J.; Meiβner D.; Kwasniewski A. *J. Non-Cryst. Solids* **2003**, *320*, 40–55.

Appendix A

The distribution and effective portion of the electrostatic energy density for our microelectrodes are simply calculated halfway between the electrodes above the surface. Considering the dimensions of our microelectrodes, only a pair of the electrodes, #1 and #1′ for instance, mainly contributes to the electric field. Furthermore, the electrodes can be assumed to be a pair of semi-infinite planes, so that the electric field is two-dimensional. As shown in Figure A1 (a), the electrodes on the x–z plane can also be

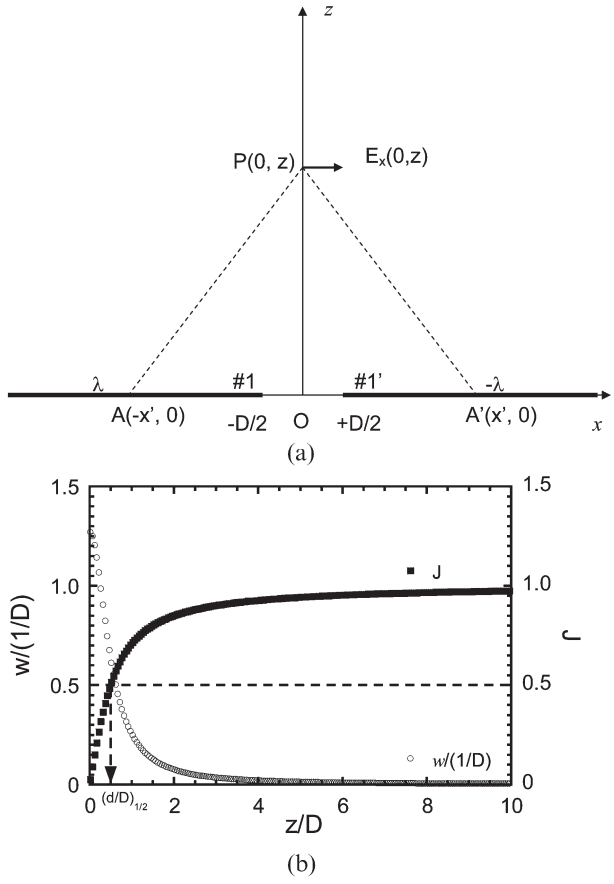

Figure A1. (a) Schematic illustration of the side view of part of electrodes #1 and #1′ shown in Figure 2 and (b) the calculated electrostatic energy density, $w/(1/D)$, and its effective portion, J, halfway between the electrodes along the $+z$ direction.

assumed to be a pair of semi-infinite line charges with charge densities λ and $-\lambda$, spaced a distance D apart. The lateral component of the electric field, $E_x(0, z)$, halfway between the electrodes above the surface, at which the vertical component of the electric field $E_z(0, z)$ disappears, is simply calculated using the following Equation:

$$E_x(0, z) = \frac{\lambda}{2\pi\varepsilon_0} \int_{+D/2}^{+\infty} \frac{x'}{(x'^2 + z^2)^{3/2}} \mathrm{d}x' = \frac{\lambda}{2\pi\varepsilon_0 D} \left[\left(\frac{1}{2}\right)^2 + \left(\frac{z}{D}\right)^2 \right]^{-1/2}, \quad \text{(A1)}$$

where ε_0 is the permittivity of free space.

The distribution of the electrostatic energy density $w(0, z)$ can be normalised (*14*):

$$w(0, z) = [E_x(0, z)]^2 \Big/ \int_0^{+\infty} [E_x(0, z)]^2 \mathrm{d}z = \frac{4}{\pi D} \left[1 + 4\left(\frac{z}{D}\right)^2 \right]^{-1} \equiv w(z/D). \quad \text{(A2)}$$

Furthermore, an effective portion of the electrostatic energy density $J(0, z)$ can also be calculated:

$$J(0, z) = \int_0^{+z} w(0, z)\mathrm{d}z = \frac{2}{\pi} \tan^{-1}\left[2\left(\frac{z}{D}\right)\right] \equiv J(z/D) \quad \text{(A3)}$$

In Figure A1 (b), $w/(1/D)$ and J are plotted against z/D. The electric field is localised near the electrode surface, and a characteristic (or penetration) depth of the electrostatic energy density above the microelectrodes is estimated at the distance $(d/D)_{1/2}$ for $J=1/2$. As shown in the figure, the characteristic depth is half the gap distance between the electrodes. (The contributions of other pairs of electrodes can also be analytically calculated for $E_x(0, z)$. The distribution and effective portion of the electrostatic energy density may be calculated numerically. The electric field was slightly more localised around the surface, but the correction was minor.) In the present study, the effective portion of the electrostatic energy density was experimentally investigated for wet films with different film thicknesses.